Memoirs of the Faculty of Engineering, Kyushu University, Vol. 71, No. 4, December 2011

Evaluation of Skin Friction of Tapered Piles in Sands based on Cavity Expansion Theory

by

Suman MANANDHAR* and Noriyuki YASUFUKU**

(Received November 5, 2011)

Abstract

On the basis of mechanism of tapered piles and evidence of small scale model tests, the cylindrical cavity expansion theory has been proposed to evaluate the skin friction of tapered piles by introducing stress-dilatancy relationship. Generally, either angle of internal friction or dilatancy angle was assumed to be constant to compute the skin friction. In this research this drawback has been removed and adopted both properties to evaluate the skin friction at each depth iteratively. The test result and proposed model show that a slight increase in tapering angle of the pile results in higher skin friction comparing with conventional straight piles on different types of sands at different relative densities. The parametric studies on different types of model tests, prototype tests and real type pile tests have been assessed to evaluate the skin friction and predict the proposed model. The proposed model validates the determination of skin friction using stress-dilatancy relation with reference to cavity expansion theory.

Keywords: Skin friction, Tapered piles, Cylindrical cavity expansion theory, Relative density, Sands

1. Introduction

The tapered pile with the difference in axial diameters at its top and bottom has merits in terms of the bearing capacity and the radial stress over conventional piles. A small increase in degree of tapering can achieve higher skin friction [1)]. There is increment of overall resistance of pile by a factor of 5-9 when mobilized towards depth however there is a negligible taper on the lateral surface of the pile [2)]. In the mean time, the mechanism of tapered piles also has good pressing effects towards the depth of penetration [3)]. However, in practice, use of tapered piles is limited and as a result very few researches have been carried out on these types of piles. These may be due to lack of awareness about basic existence together with lack of modern and reliable analytical method for estimating its bearing capacity [4)]. The analytical method was applied to evaluate the axial capacity of the tapered piles over straight piles when the tapered piles were driven into

*Post Doctoral Fellow, Department of Civil and Structural Engineering
** Professor, Department of Civil and Structural Engineering

cohesionless soil [5]. Nevertheless, the accurate model to derive the axial capacity of the tapered pile in context to deep foundation was not well identified. Some pioneer geotech proposed the theoretical methods on geomechanics with specialization in cavity expansion theory [6-9]. The most closed form solution for large straining condition and complete solution for cylindrical cavity expansion in ideal elastic-plastic model in non-associated flow rule postulated by Yu and Houslby (1991), has been well adopted by researchers after comparing with other researchers [10]. In general, one of the soil parameters (angle of internal friction or dilatancy angle) is assumed to be constant for the ease in computation. However, stress-dilatancy relationship is interdependent on the confining pressure, relative density and angle of internal friction. Therefore, the new concept is proposed to unify the idea proposed by Kodikara and Moore (1993) and cavity expansion theory to estimate the skin friction of tapered piles by introducing stress-dilatancy relation reported by Bolton [11-12]. In the proposed stress-dilatancy relationship, the increase of confining pressure will increase relative density along with increasing angle of internal friction and dilatancy. All these parameters are successfully introduced in the cavity expansion theory propounded by Yu and Houlsby (1991) and has made possible to compute at each segment of pile during pile penetration [13]. In this research axial cylindrical pile loading tests have been considered in the model tests to understand the mobilized mechanism and behavior at certain depth in which size effects is not considered.

2. Mechanism of pile loading

When pile is penetrated in a downward frictional mode, the failure zone is developed along soil-pile interface by partly upheaving the surface to certain depths. Below the critical depth the horizontal displacement occurs by compressing soil elastically and partly consolidating around the interface. In case of sand of medium density, a thin layer of soil particles drag along and compress the layers along lateral directions. It has been reported that the diameter of the disturbed zone around the pile was approximately six times the diameter of the pile in which the displacements had decreased according to a parabolic law [14]. Therefore, in this section, small model chamber pile load tests were carried out understand the mobilized mechanism of piles. Three different types of steel chromium piles, one straight (S′) and two tapered (T_1' and T_2') have been considered to perform tests on Toyoura (TO) sand at 80 % relative density. The detail procedures are written in the previous paper of this bulletin which is focused especially to check the end bearing mechanism at the same chamber. 3.234 kPa overburden pressure has been supplied to this very small model chamber (**Fig. 1**) at speed of 4 mm/min up to 100 mm. After loading, the modeled ground was trimmed and interprets visually (**Fig. 2**).

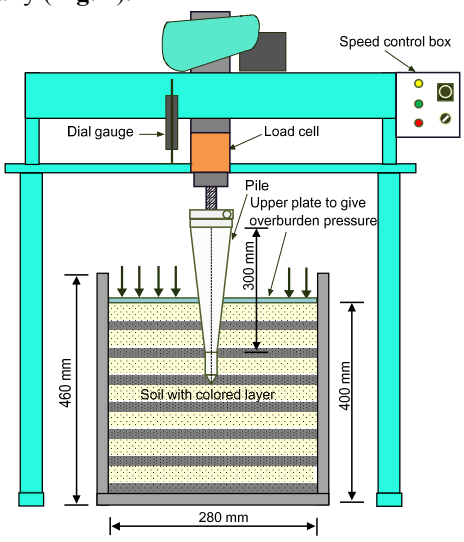

Fig. 1 Schematic diagram of pile load test apparatus for the mobilized mechanism (figure is not in scale).

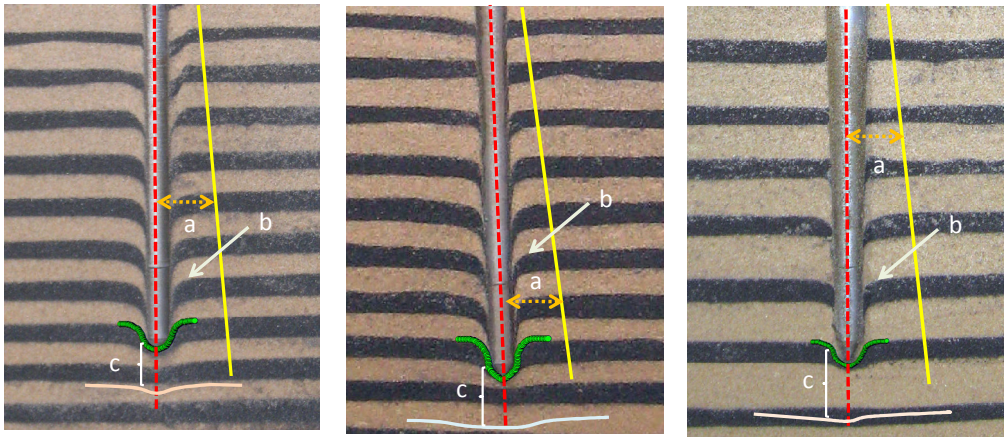

Fig. 2 Mobilized mechanism of pile: a = effective length of influenced zone; b = convex heave due to effect of pile; c = effective length at the pile tip settlement.

2.1 Visual interpretation of skin friction

The visual inspection and measurements of dimensions of disturbed soil particle zone have been carefully observed. Here, the failed zone is named as influence and the measurements have been made from the center of the pile termed as radius of influenced zone in this study. After the pile penetration, the affected area around the shaft was measured from the center of the pile to the visually affected radius. Straight pile showed the minimum radius of influence with compared to tapered pile. The measurement of effective radius of influence shows the increase of influence area with increase in the degree of tapering of piles. At the same time, convex heave on pile-ground interface has been narrowed and decreased in tapered piles. This is because of increase in horizontal stresses with the degree of tapering as shown by **Fig. 2**. All the radius of influences of maximum and minimum zones were measured and mean of influenced area were plotted for all piles as shown by **Fig. 3**. It shows that the straight pile has lowest radius of influence while the most tapered pile received highest influence with relation to increase in lateral stresses radially. Hence, visual inspection of mobilized mechanism gives strength to increase skin friction as well as lateral pressure during pile penetration to minimize the failure zone effectively. In order to support the mobilized mechanism of different piles, relatively large model tests have been carried out in which skin friction and lateral stresses around the pile can easily be understood and give strength to the visual interpretation of small pile model tests.

3. Evidence of model tests

3.1 Sample preparation and test procedures

The model tests of different piles have been facilitated by two different types of simulated ground using two different types of air-dried sands, K-7 sand and typical Toyoura sand. The chromium plated steel model piles with equal lengths of 500 mm and same tip diameters of 25 mm were used for pile penetration. One straight (S) and two tapered piles (T-1 and T-2) were used for the model pile load tests which have load cell at the tip to measure load connected by cord. For convenience, the configuration of the chamber is shown by **Fig. 4**. The detail geometrical configuration and geotechnical properties are adopted from Manandhar [13] and included in the previous paper of this bulletin which has been focused on end bearing capacity of tapered piles in sands using cavity expansion theory.

In order to prepare the model ground, the maximum and minimum dry densities of K-7 and Toyoura sands were determined by the method proposed by Japanese Industrial System (JIS A 1224) and Japanese Geotechnical Standards (JGS 0161) [15]. The relative density (I_D) 60 % of K-7

sand and 80 % of TO sand were calculated accordingly. A sample preparation method using multiple sieving can give a wide range of specimen density by height of fall and nozzle diameter [16]. Thus, air-dried silica sand was fallen freely through sieve on determined height. K-7 sand was fallen freely from the height of 1400 mm on the chamber by rotating homogenously where as TO sand was fallen at the controlled height of 700 mm. Then, at first, soil was filled nearly 710 mm from the bottom and pile was set up at the centre of the chamber. Then, four transducers were set up at the equal interval of 60 mm from one to another. First transducer was installed close to pile tip which measure the lateral earth pressures. From the center of the pile earth pressure sensors 1, 2, 3 and 4 were installed at 30 mm, 90 mm, 150 mm, and 210 mm respectively. Further, soil was poured up to 930 mm from the bottom of the chamber.

Finally, pneumatic air pressure of 50 kPa was set up as the overburden pressure (σ_v) vertically. Then pile was penetrated down up to 200 mm as initial preparation phase of pile model test at the rate of 5 mm/min and kept for 15 hours for stress relaxation to settle down the pile in the ground. Afterwards, pile load test was carried out up to settlement ratio of 0.4 to facilitate as bored pile.

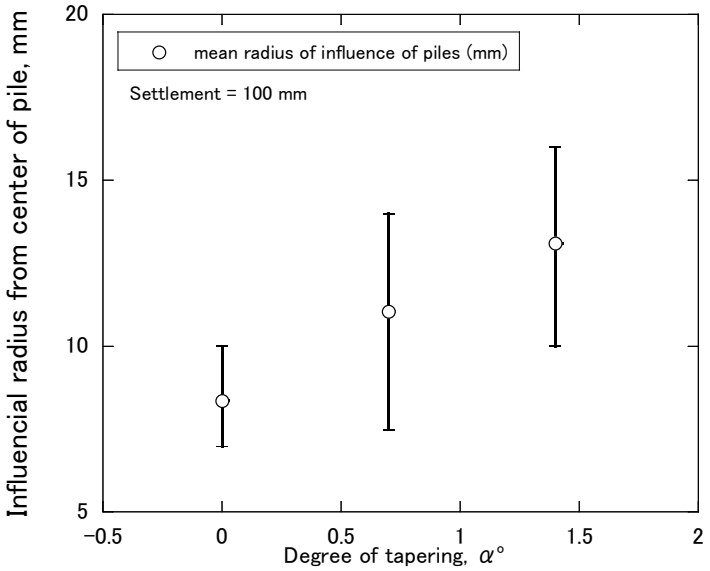

Fig. 3 Visually measured radius of influence of skin friction of piles.

3.2 Test results

The model pile load test has an advantage that the loads at pile tip, pile head and lateral earth pressure can be directly measured during experiment. The differences of load at pile head and pile tip gives the skin friction on the shaft of piles which can be expressed as:

$$P_S = P_T - P_B \tag{1}$$

Figure 5 represents the total skin frictions of K-7 and Toyoura sands under different piles, the tapering effects of piles were shown to be higher with increasing skin friction. With increasing the tapering angle the load were gradually increased in a considerable amount at high normalized settlement ratio. Here, S is considered as settlement and D is the pile tip diameter. During pile penetration, the surface area affects the unit skin friction (f_s). Hence the unit friction is generally obtained by dividing surfaced area of pile to the skin friction such that:

$$f_s = \frac{P_S}{A_S} \tag{2}$$

$$A_s = \pi D_{av}(L + \Delta L) \tag{3}$$

$$D_{av} = \frac{D_t + d}{2} \quad (4)$$

Here, D_{av} is the average diameter of pile head (D_t) and pile tip (d), L is the effective length of pile and ΔL is the incremental depth of pile penetration expressed in metric system.

The unit skin friction ratio has remarkably increased from the beginning of pile penetration in both K-7 and TO sands respectively as shown by **Fig. 6**. In this figure, both grounds receive remarkable high skin frictions when degree of tapering angle is increased. If observe carefully, it is well known that however different sands with different fine contents are subjected in different settling environment, tapered pile shows the similar trend. In addition, the mechanism of the skin friction can be compared with conventional piles by taking ratios of skin friction of tapered pile.

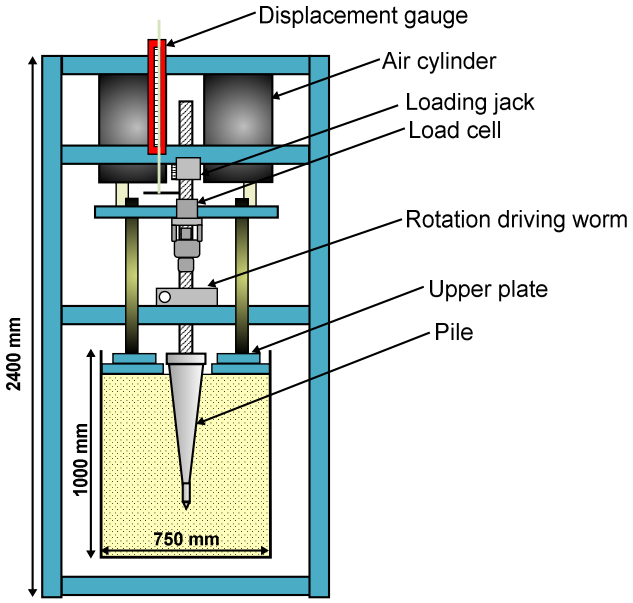

Fig.4 Geometry of the pile loading test apparatus (figures are not in scale).

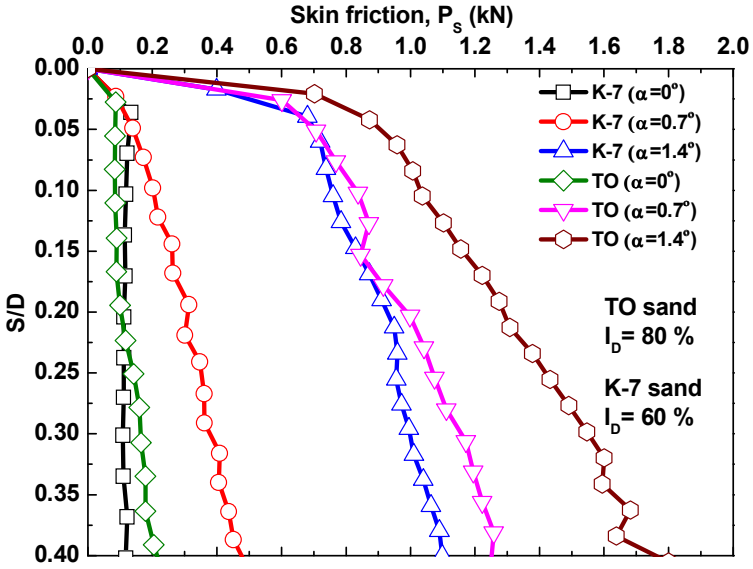

Fig. 5 Total skin friction of piles on K-7 sand and TO sand.

Figure 7 explains that the unit skin friction ratios of the most tapered pile at 0.4 settlement ratios have increased. When settlement ratio 0.1 has been taken, the unit skin friction ratios have increased in both sands. These evidences from small model tests clearly show the benefits of tapered piles. Based on these evidences, the evaluation method needs to find the total bearing capacity. The proposed models and liability will be discussed with prototype and real pile references in the next section.

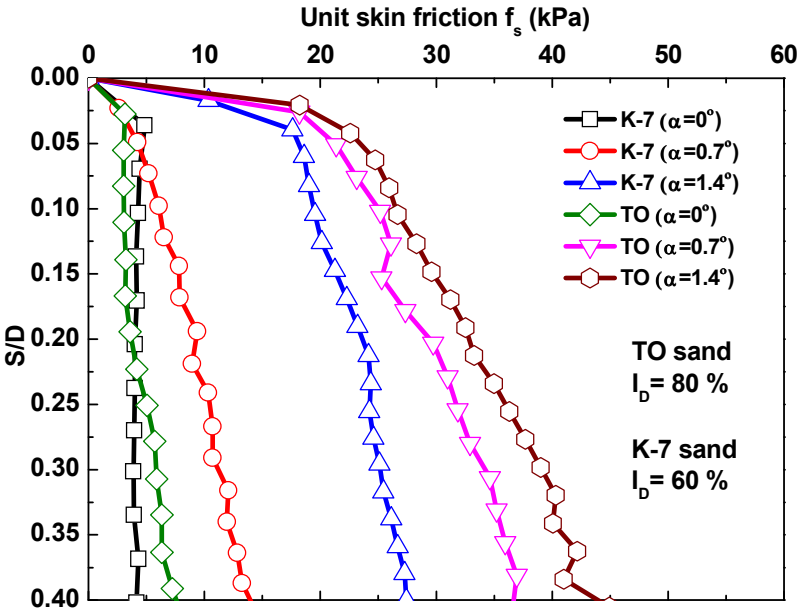

Fig. 6 Unit skin frictions of K-7 sand and TO sand.

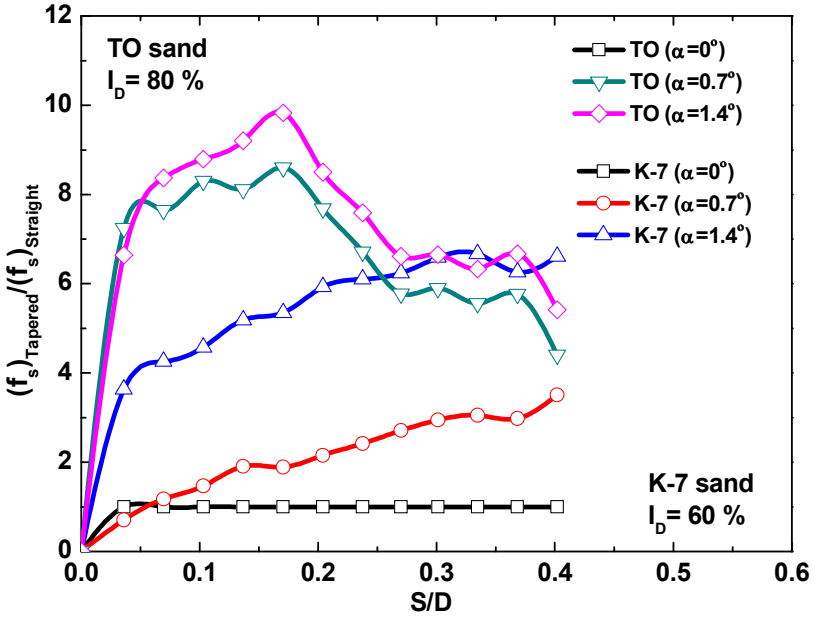

Fig. 7 Unit skin friction ratios of K-7 sand and TO sand.

3.3 Effects of lateral pressure

The model pile load test has facilitated with installation of lateral earth pressure transducer in order to see the behavior of stress conditions around the pile-ground interface and away from the pile in the chamber radially. At the symmetry, only one direction is sufficient to observe the stresses around the effective region. Radial distance from the center of the pile was normalized by dividing distance of transducers to the pile tip radius (r/r_n). Since the design considers in 0.1 settlement ratios, the effects of stress aroused during pile loading was carefully traced as shown schematically in **Fig. 8**. **Figure 9** (**a** and **b**) shows the effects of radial earth pressures at the pile tip during pile penetration up to 0.4 settlement ratio. Figures show that near the pile-ground interface, the stresses are highly developed. When observe away from the pile-ground interface, the influence of piles are decreased in large quantity. In addition, if the influence of this lateral stress is carefully checked in the context to different types of piles, the mobilized mechanism can clearly be understood. TO sand obtains more than 3 times high lateral stress at the pile-ground interface when the most tapered pile T2 was penetrated at 0.1 displacement ratio while compared with straight cylindrical pile. Similarly, K-7 sand also shows such patterns however the increment value differs due to different ground density. Here, it is clearly seen that the compressibility of sand increases near the pile-ground interface. Higher the density, greater the influence on distribution of lateral earth pressures. Moreover, the lateral earth pressure adjacent to first earth transducer shows drastic fall down of lateral earth pressure and tends nearly to zero value however it is very near from the center of the pile. This may indicate the movement of soil particles towards the pile in greater amount. This assumption has given strength in the small model tests in previous section to understand the mobilized mechanism of different types pile showing the tapering effects.

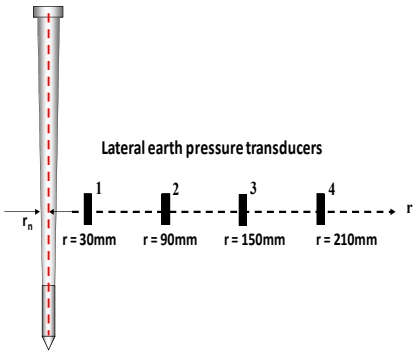

Fig. 8 Radial distance from the center of the pile normalized by dividing distance of transducers to the pile tip radius (r/r_n).

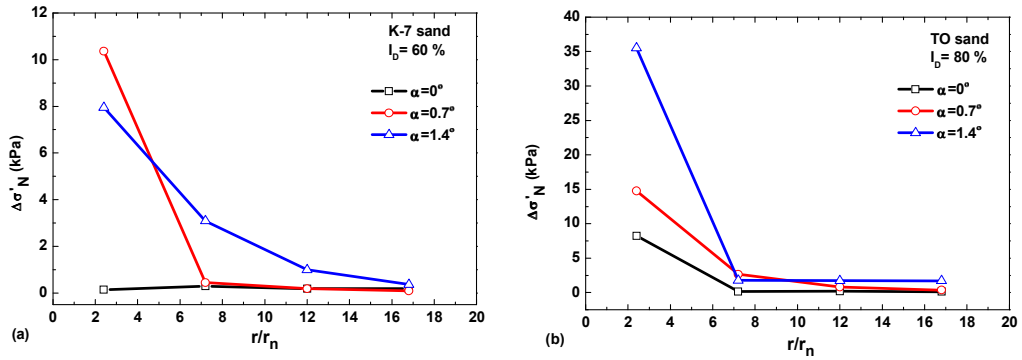

Fig. 9 Lateral stress distribution at 0.1 settlement ratio at (a) K-7 sand and (b) TO sand.

4. Evaluation of skin friction using cavity expansion theory

The results of mobilized mechanism of small model tests and relatively large pile model test have shown that the skin friction has increased with increasing tapering angle. The experimental evidence showed that maximum tapered pile in the study has increased the compressibility and lateral earth pressure of the ground when the pile was penetrated downward in a frictional mode. With respect to these benefits, it is important to give the evaluation technique to compute the skin friction of tapered piles. In this paper, cavity expansion theory will be discussed along with stress-dilatancy relationship to measure the skin friction in the closed form.

4.1 Stress-dilatancy relationship and cavity expansion theory

The soil is presumed to be dilated plastically at a constant rate [17]. The non-associated flow rule is well established for modeling dilatants soils with the Mohr-Coulomb yield criterion. Generally, zero dilatants angle has been considered to compute large strain analyses. In reality, the angle of internal friction and the rate of dilation towards the critical state is the function of both density and effective stress which cannot be avoided in the computational procedure however it is more complex during calculation. In addition, density and confining pressure undergo change when tapered piles penetrate with settlement ratios. Confining pressure increases with increasing relative density together with angle of internal friction and dilatancy. The stress-dilatancy relation established by Bolton [11-12] has been introduced in Yu and Houlsby's cavity expansion theory [8] to check the bearing behavior of different piles.

For a plane strain, the stress-dilatancy relation can be expressed in the following term:

$$\phi'_{max} - \phi'_{cv} = 0.8\,\psi_{max} = 5\,I_R^o \tag{5a}$$

$$I_R = I_D(10 - ln\,p') - 1 \tag{5b}$$

Where, ϕ'_{max}, ϕ'_{cv}, ψ_{max}, and I^o_R are maximum angle of friction, angle of friction at critical states, maximum dilation angle and relative dilatancy index at plane strain respectively. The relative dilatancy index I_R is a function of relative density I_D and mean effective stress p' as shown in Eq. (5b). The mean effective stress can be simply defined as the mean radial and hoop stresses explained in the cavity expansion theory as follows:

$$p' = \frac{\sigma_r + \sigma_\theta}{2} \tag{5c}$$

A plastic zone will be formed after an initial yielding takes place at the cavity wall within the region $a \le r \le b$ with increment of cavity pressure p. Separating elastic and plastic regions, it will be easier to understand the behavior clearly.

The stress component at the plastic region satisfying the equilibrium condition can be obtained as following expressions respectively:

$$\sigma_r = \frac{Y}{\alpha' - 1} + Ar^{-\frac{(\alpha'-1)}{\alpha'}} \tag{6}$$

$$\sigma_\theta = \frac{Y}{\alpha' - 1} + \frac{A}{\alpha'} r^{-\frac{(\alpha'-1)}{\alpha'}} \tag{7}$$

Where, A is a constant of integration. Derivational procedures are shown detail in Appendix I.

Substituting the values of σ_r and σ_θ from Eqs. (6) and (7) into Eq. (5c) to obtain the following relation as:

$$p' = \frac{1}{2}\left[\frac{Y}{\alpha' - 1} + Ar^{-\frac{(\alpha'-1)}{\alpha'}} + \frac{Y}{\alpha' - 1} + \frac{A}{\alpha'} r^{-\frac{(\alpha'-1)}{\alpha'}}\right] \tag{8a}$$

Replacing the constant of integration A, the above equation is simplified into the following form as:

$$p' = -p_0 b^{\frac{(\alpha'-1)}{\alpha'}} r^{-\frac{(\alpha'-1)}{\alpha'}} \tag{8b}$$

The general Eq. (8b) can be simplified in the elastic-plastic region. At the boundary of plastic region where $r \leq a$, the effective mean stress can be modified into the following structure as:

$$p' = -p_0 R \tag{9}$$

4.1.1 Settlement of pile

Kodikara and Moore [10] have established the deformation behavior of a compressible elastic pile through differential equations assuming the equilibrium condition. The elastic deformation of pile during pile penetration in certain depth is quite negligible and almost equal to settlement. Therefore, in this section pile deformation behavior is considered as settlement of pile. Consider a small horizontal section of thickness dx in **Fig. 10** as:

$$\frac{dF_x}{dx} = 2\tau_x \pi r_x \tag{10}$$

Where at depth x, F_x is the axial force, τ_x a function of the settlement of the pile u_p and the vertical component of the stress at the pile-ground interface, and r_x is the pile radius. Constant taper angle α and mean pile radius along the embedded length r_m can be expressed for embedded length of the pile L as:

$$r_x = r_m + \left(\frac{L}{2} - x\right) tan\alpha \tag{11}$$

The axial strain of the pile can be equated to the axial load obeying Hooke's law:

$$\frac{du_p}{dx} = \frac{F_x}{A_1 E_p} \tag{12}$$

Where, A_1 is the cross-sectional area of the section and E_p is the Young's modulus of the pile material. Then, combining Eqs. (9), (10) and (11), it can be arranged the relationship as:

$$\frac{d^2 u_p}{dx^2} = \frac{2tan\alpha}{\left[r_m + \left(\frac{L}{2} - x\right) tan\alpha\right]} \frac{du_p}{dx} = \frac{2\tau_x}{\left[r_m + \left(\frac{L}{2} - x\right) tan\alpha\right] E_p} \tag{13}$$

With relation τ_x-u_p, the pile settlement behavior can be solved using Eq. (13).

4.1.2 Skin friction

This section determines the skin friction of piles into three zones based on settlement behavior. At first, an elastic deformation when pile-ground interaction bonded together. Second, when slip has occurred at the pile-ground interface and ground still behaves elastic deformation. And third, when slip has occurred and plastic zone has developed to obtain elastic perfectly plastic pile-ground interface.

For small tapering angles ranges from 0° to 5°, similar to cylindrical piles, behaves as initial elastic deformation. Therefore, it is reasonable to approximate the deformation behavior of the ground by the theory of concentric cylinder shearing [18].

The vertical displacement of ground u_g and expression for the Poisson's ratio can be expressed in terms of the mean radius of the pile r_m as:

$$u_g = \zeta \frac{\tau_x r_m}{G} \tag{14}$$

$$\zeta = ln\left[\frac{2.5\,L(1-v)}{r_m}\right] \tag{15}$$

In this region the settlement of pile and ground are same so that the τ_x-u_p relation is altered in as follows:

$$\tau_x = \frac{G}{\zeta r_m} u_p \tag{16}$$

This equation will continue until the pile-ground interface reaches the yield. Assume shear stress τ_0 belongs to this phase. At this condition, it is assumed that no significant increase in the radial stress acting on the pile wall occurs.

Assuming the small section of the pile as shown in **Fig. 11 (a)**, the stresses acting normal and parallel to the pile-ground interface respectively are shown by σ_n and τ_n as:

$$\tau_n = \sigma_n tan\left(\phi_i + \alpha\right) + c_i \tag{17}$$

The vertical and radial components of the stresses at the interface (τ_0 and σ_0) govern this state in the form:

$$\tau_0 = \sigma_0 tan\left(\phi_i + \alpha\right) + \frac{c_i\, sec^2\,\alpha}{(1-tan\,\alpha\, tan\,\phi_i)} \tag{18}$$

Where, ϕ_i and c_i are the friction angle and the cohesion at the pile-ground interface respectively.

When slip occurs at the pile-ground interface and the vertical pile movement u_p at any point X on the pile-ground interface is greater than the vertical ground movement u_g at the corresponding point Y on the interface. As shown in **Fig. 11 (b)**, pile displaced from point X to X' while at the same time, ground moves from point Y to Y' in such a way that the component of lateral movement (radial expansion) v, can be determined in the form:

$$v = \left(u_p - u_g\right) tan\alpha \tag{19}$$

For small taper angles, the increase in radial stress $\Delta\sigma$ for radial expansion may be calculated from cylindrical cavity expansion theory. The following expression is obtained using the mean pile radius r_m and assuming the ground behaves elastically.

$$\Delta\sigma = K_e v \tag{20}$$

$$K_e = \frac{2G}{r_m} \tag{21}$$

When the pile-ground continuously yields, the vertical shear stress τ_x acting on the pile wall can be expressed as:

$$\tau_x = (\sigma_0 + \Delta\sigma) tan\left(\phi_i + \alpha\right) + c_i' \tag{22}$$

Where,

$$c_i' = \frac{c_i\, sec^2\,\alpha}{(1-tan\,\alpha\, tan\,\phi_i)} \tag{22a}$$

In Eq. (19), the ground deformation u_g may be related to shear stress τ_x by the relation given in Eq. (14). Using this approximation and Eqs. (19), (20), and (22), the τ_x-u_p relationship for this phase can be written as:

$$\tau_x = \frac{K_e\, tan\,\alpha\, tan(\phi_i+\alpha) u_p + \sigma_0\, tan(\phi_i+\alpha) + c_i'}{1+\frac{K_e \zeta r_m}{G} tan\,\alpha\, tan(\phi_i+\alpha)} \tag{23}$$

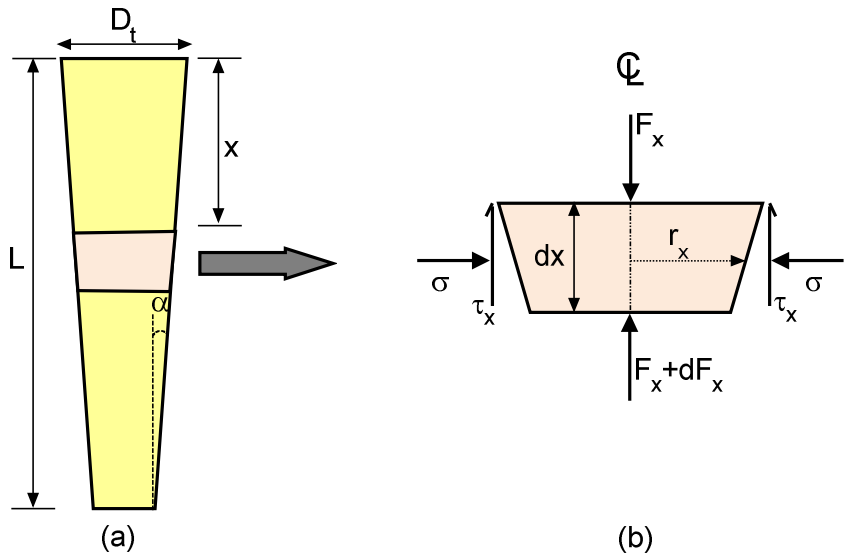

Fig. 10 Geometry of tapered pile **(a)** complete section; and **(b)** segment at depth x.

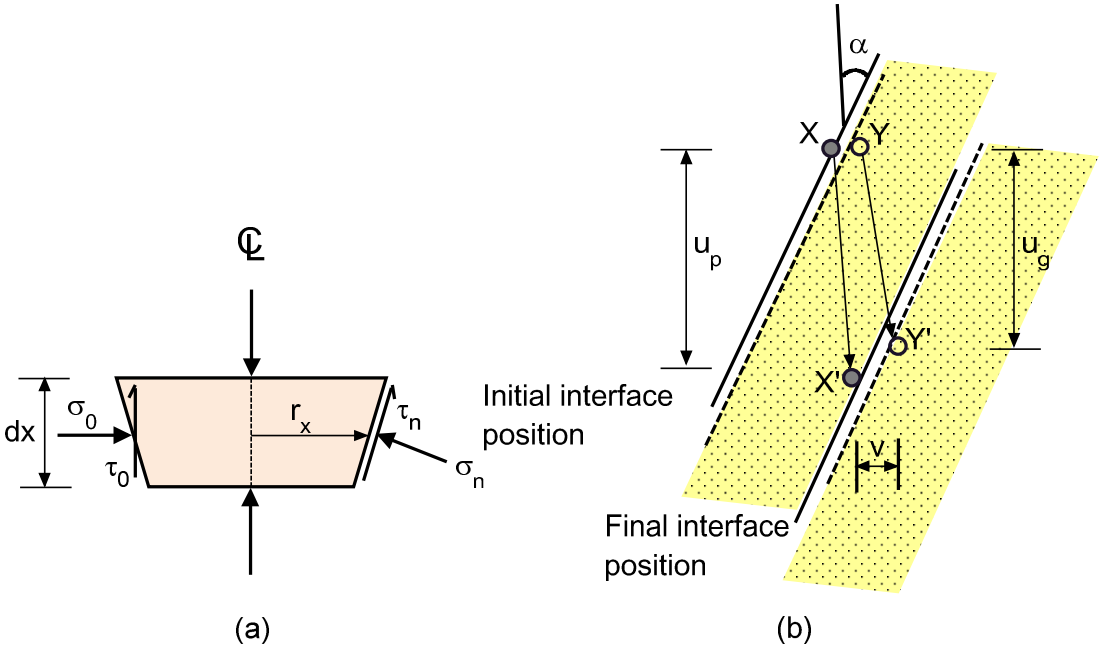

Fig. 11 (a) Segment of pile-ground interface; and **(b)** kinematics of initial and displaced position.

This equation is applicable until the ground starts yielding at the pile-ground interface. Assuming a Mohr-Coulomb yield criterion, the radial stress at this point can be expressed as:

$$\sigma_Y = \sigma_0(1 + sin\ \phi) + c\ cos\ \phi \tag{24}$$

Proceeding, the pile deformation $(u_p)_Y$ at ground yield can be expressed as:

$$(u_p)_Y = \frac{\sigma_0}{K_e} cot\alpha \left[(1 + sin\,\phi)\left(1 + \frac{K_e \varsigma r_m}{G}\right) tan(\phi_i + \alpha)\, tan\alpha - 1\right] + \frac{c}{K_e} cos\,\phi cot\,\phi \left[1 + \frac{K_e \zeta r_m}{G} tan(\phi_i + \alpha)\, tan\,\alpha\right] + \frac{\zeta r_m}{G} c_i' \quad (25)$$

When $(u_p > (u_p)_Y)$ or $\sigma > \sigma_Y$, it indicates a plastic zone adjacent to pile wall. In this case it will explain the influence of plastic zone which will extend further with more pile deformation. As noted in Eq. (20) it is important to compute the tangent gradient of cavity stress to cavity radius during the expansion. The expression for this gradient (K_p) has given by solution Yu and Houlsby [9] as follows:

$$K_p = \frac{1}{A}\frac{1}{C}\frac{\beta+1}{\beta}\left(\frac{a}{a_0}\right)^{(\beta+1)/\beta}\frac{1}{a} \quad (26)$$

Where,

$$A = \frac{(\alpha'+1)(\alpha'-1)}{2\alpha'\left[Y + \left((\alpha'-1)\sigma_0\right)\right]} \quad (27)$$

$$C = \frac{-\gamma D R^{-\gamma-1} + \frac{\gamma}{\eta} R^{-\gamma} \frac{d\Lambda(R,\xi)}{dR}}{D^2} \quad (28)$$

$$D = \left[(1-\delta)^{\frac{(\beta+1)}{\beta}} - \frac{\gamma}{\eta}\Lambda(R,\xi)\right] \quad (29)$$

$$\Lambda(R,\xi) = \sum_{n=0}^{n=\infty} P_n \quad (30)$$

in which,

$$P_n = \begin{cases} \frac{\xi^n}{n!} ln\, R, & if\ n = \gamma \\ \frac{\xi^n}{n!(n-\gamma)}\,(R^{n-\gamma} - 1), & otherwise \end{cases} \quad (31)$$

and hence,

$$\left[\frac{a}{a_0}\right]^{(\beta+1)/\beta} = \frac{R^{-\gamma}}{(1-\delta)^{(\beta+1)/\beta} - \frac{\gamma}{\eta}\Lambda(R,\xi)} \quad (32)$$

At this phase, a small increment in radial stress ($d\sigma$) can be written as:

$$d\sigma = K_p dv \quad (33)$$

Where,

$$dv = \left(du_p - du_g\right)\, tan\,\alpha \quad (34)$$

Integrating (34) and using (14), it gives:

$$v = u_p\, tan\,\alpha - \frac{\zeta r_m}{G} tan\,\alpha\, \tau_x \quad (35)$$

Integrating (33), the radial stress (σ) can be expressed as:

$$\sigma = \sigma_Y + \int_{vY}^{v} K_p\, dv \quad (36)$$

Where, v_Y can be computed from (36) using $(u_p)_Y$ and $(\tau_x)_Y$ which is vertical shear stress in Eq. (23) when $u_p=(u_p)_Y$. Then, the corresponding vertical shear stress, τ_x can be expressed as:

$$\tau_x = \left(\sigma_Y + \int_{vY}^{v} K_p\, dv\right) tan\left(\phi_i + \alpha\right) + c_i' \quad (37)$$

This Eq. (37) gives the skin friction at certain depth. For a solution of complete pile, when both base and skin resistances operate, it is necessary to include the boundary condition at the base resistance as $x = L$, whose development will be similar to that of a cylindrical pile. The base resistance can be represented by an elastic spring manner similar to Murff [19]. Following Randolph and Wroth [17], the base of pile can be assumed to be similar to a rigid punch which can be expressed as:

$$\frac{F_b}{(u_p)_b} = \frac{4r_b G}{(1-\nu)\eta_b} \tag{38}$$

Where, b is the parameter used at the base and η_b is the coefficient introduced to allow for the depth of the pile base below the surface.

4.2 Numerical solution of the model

The load transfer method proposed by Coyle and Reese [20] (based on the work of Seed and Reese [21]) is accomplished and proposed stress-dilatancy relation has been introduced in the numerical analyses. In this technique, pile is divided into number of small segments and characterized these elements with pile-ground interface in order to find the vertical shear stress, horizontal stress along with pile settlement ratio. During analyses, small settlement at the pile base is specified and the axial load at the top of this segment is iteratively regulated to satisfy the equilibrium condition. After obtaining equilibrium condition, the process undergoes to next segment and settlements are calculated. Every possible functions such as v, shear modulus, stress-dilatancy relations are successfully computed by means of iterative techniques. **Figure 12** illustrates the flow chart of numerical solution of the proposed model and Appendix II explains the procedures in detail.

4.2.1 Results of the model

There are four various types of soil and pile materials which have been drawn on complex mathematical analyses. Three different types of soil with various relative density and confining pressures have been accomplished for data interpretations. Properties of Toyoura (TO) sand, K-7 sand and Fanshawe brick sand have been taken into consideration. Proceeding, parameters of Fanshawe brick sand and pile materials have been adapted from Sakr et al. [22-24]. The detail descriptions are included in the previous paper of this bulletin when using the same parameters are used as a reference.

Figure 13 shows the results of average vertical shear stress of the normalized pile settlement at 0.4 ratios. Same piles penetrated in K-7 sand and Toyoura sand at different relative densities illustrate clearly that the average vertical shear stresses increase with increasing tapering angle on the similar trend. **Figure 14** shows that tapering effects are higher in the case of high pressure rather than in low pressure for the determination of average vertical shear stress of Fanshawe brick sand when same higher relative density has been used. It also follows the similar trend as shown by K-7 sand and TO sand.

In order to analyze the model concretely, unit normalized skin friction was determined by dividing the unit skin friction (f_s) of tapered pile into straight pile with respect to pile settlement. If different settling environments are used with same vertical stress, higher density ground receives the greater unit normalized skin friction as shown by K-7 sand and TO sand in **Fig. 15**.

Further, the cavity expansion reduced with increment of initial radial stress at same settling environment which is satisfied by **Fig. 16** when unit normalized skin frictions were plotted with respect to pile settlement in Fanshawe brick sand. The unit skin friction normalized with average radial and vertical stresses are shown in **Fig. 17**. Normalized ratios show that measured skin frictions govern peaks before 0.1 settlement ratio and increased with increasing tapering angle. But the increasing rate after 0.1 settlement ratio is almost constant.

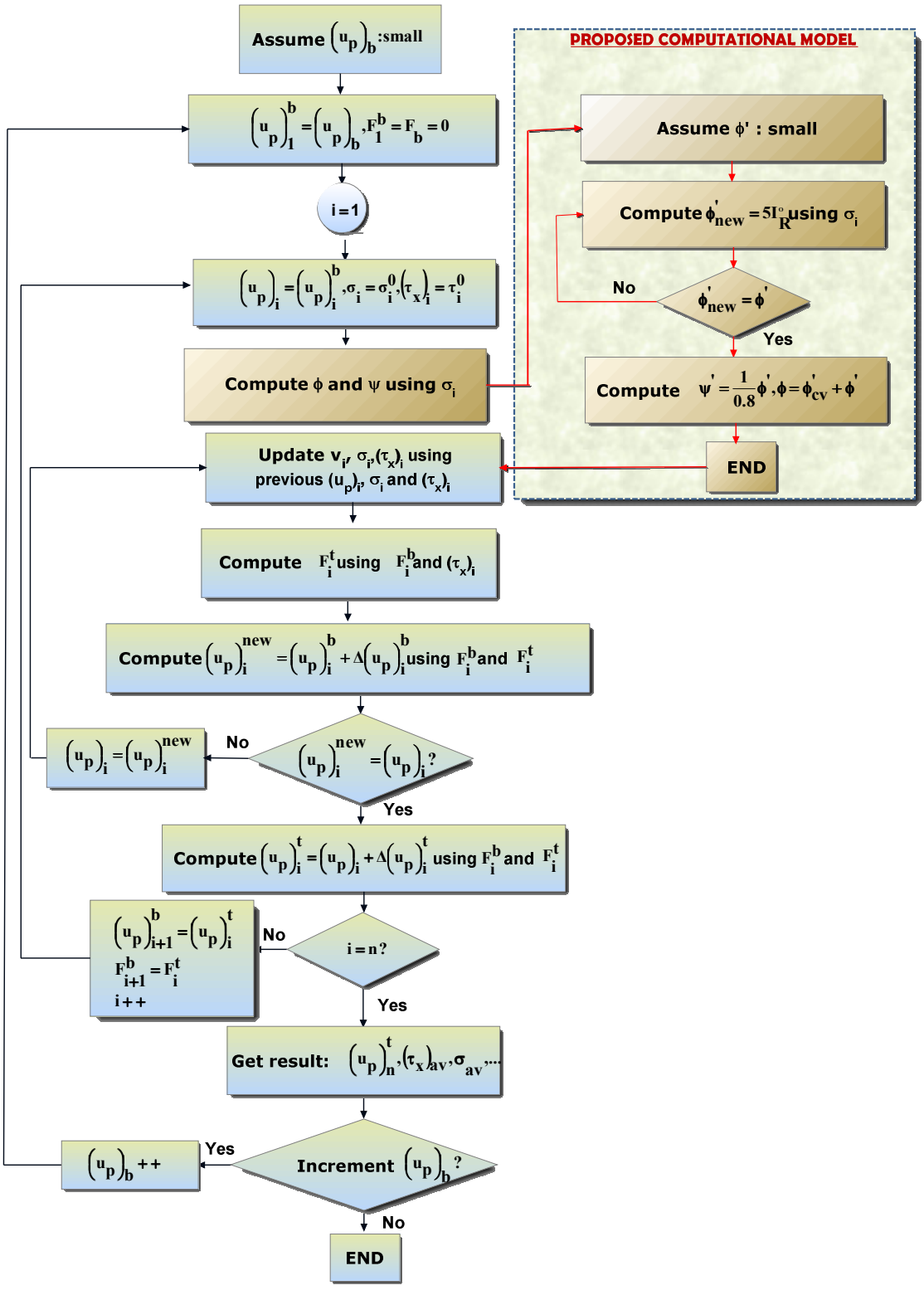

Fig. 12 Flow chart of numerical solution of the proposed cavity expansion theory.

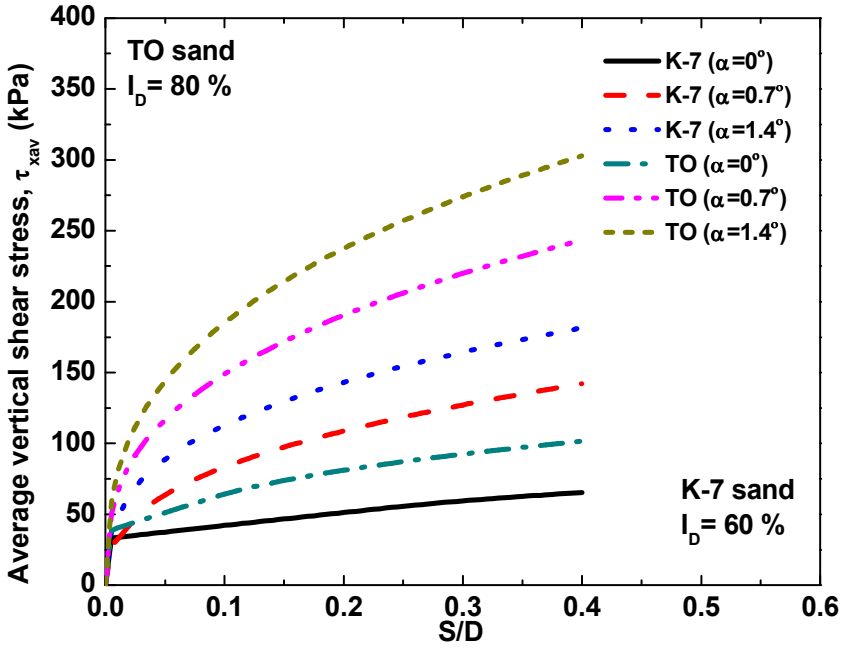

Fig. 13 Average vertical shear stress of K-7 and TO sands at different pile tapering angle at normalized settlement ratio.

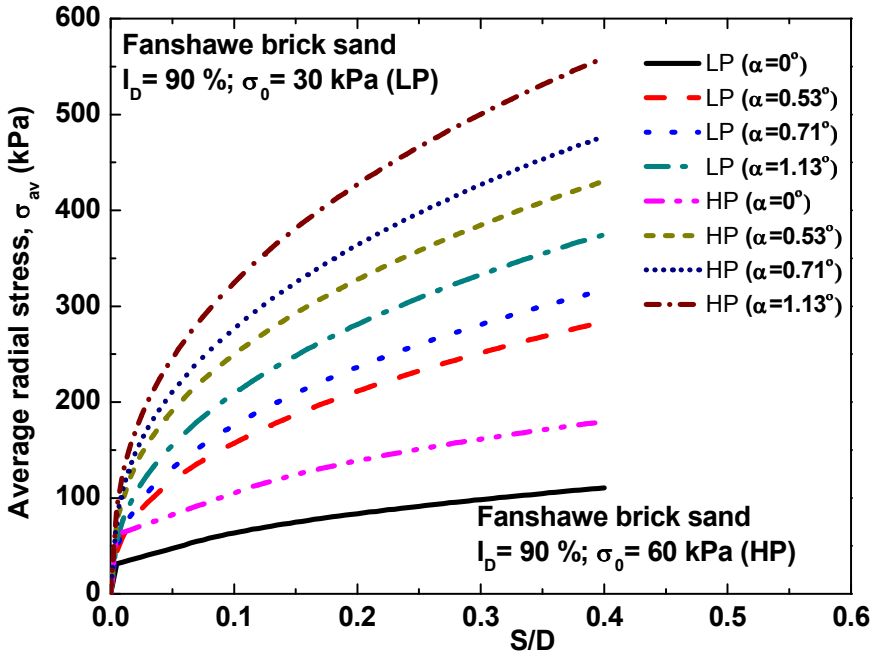

Fig. 14 Average radial stress of Fanshawe brick sand at low and high pressures and different pile tapering angle at normalized settlement ratio.

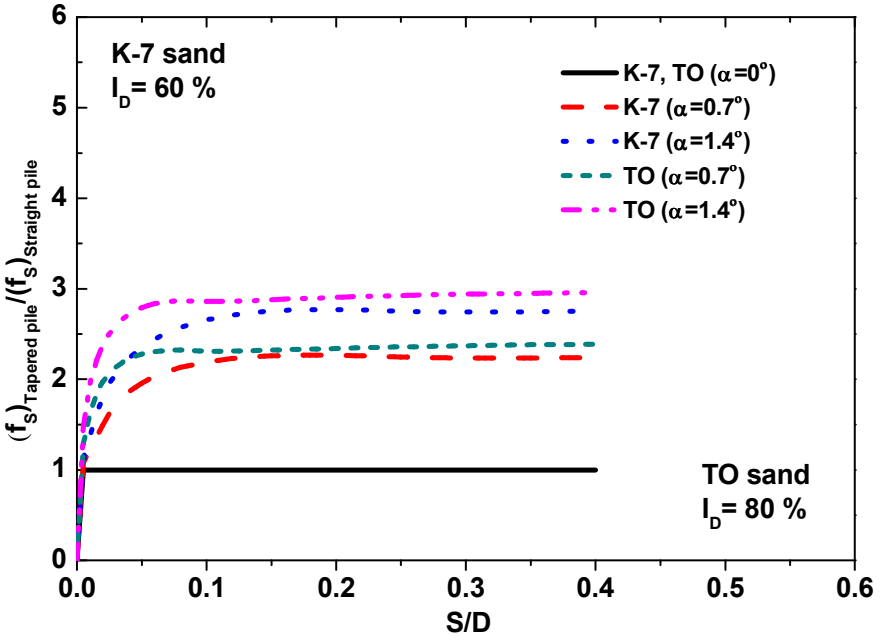

Fig. 15 Unit normalized skin frictions of K-7 and TO sand.

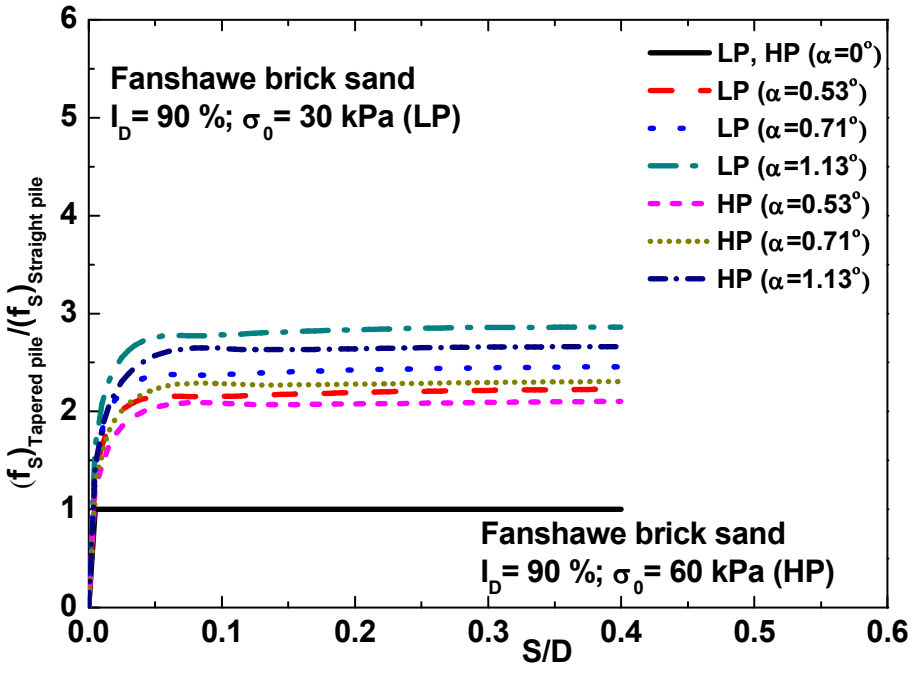

Fig. 16 Calculated unit normalized skin friction of Fanshawe brick sand at low and high pressures.

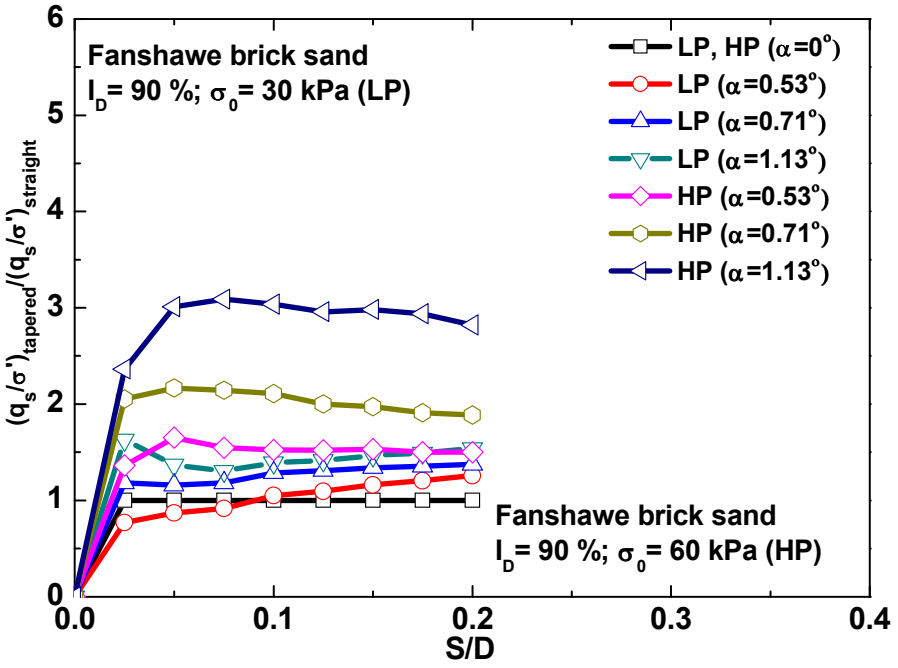

Fig. 17 Measured unit normalized skin friction of Fanshawe brick sand at low and high pressures.

5. Parametric study

The parametric studies include different types of effective key variables such as angle of tapering, distribution of the effective radial stress, relative density and stress-dilatancy relationship to understand the pile behavior in sands. Model tests, prototype test described by Sakr et al. [22-24] and El Naggar et al. [26-27] and real type Rybnikov [28] pile have been used for study. The top and bottom radii of Rybnikov [28] piles were 200 mm and 100 mm (1.2° tapering angle), one tapered pile with corresponding radii of 250 mm and 100 mm (2° tapering angle) and for last two tapered piles had radii of 300 mm and 100 mm (2.4° tapering angle) respectively.

Figure 18 shows the effect of tapering angle in four types of soil and pile materials by taking the ratios of average vertical shear stress of tapered and average vertical shear stress of straight pile. In figure, the most tapered angle shows 236 % increase in Fanshawe brick sand, 331 % in K-7 sand, 287 % in TO sand and 295 % increase by Rybnikov pile on sandy ground respectively.

The parametric study on effects of radial stress on TO sand in **Fig. 19** explains that distinct decrease of normalized unit skin friction with increase of initial radial stress hence by reducing the cavity.

Similarly, the parametric study on effect of relative density in **Fig. 20** illustrates that relatively low density ground receives low normalized average vertical shear stress when same radial stress had applied. With reference to the relative density of 0.6 at normalized settlement ratio 0.1, the normalized skin friction at relative densities of 0.8 and 0.9 had increased by 13 % and 16 % respectively. On the other hand, at 0.4 settlement ratio, the normalized skin friction had been increased by 15 % and 20 %.

Proceeding, the effect of dilatancy in **Fig. 21** shows that the Rybnikov pile material has been affected by dilation angle in side resistance. At 0.1 displacement ratio, the normalized side resistance had increased 30 % when dilation angle is 5° and 61 % when dilation angle was increased to 10° with reference to zero dilation in which angle of friction reduced to its critical state condition. Similarly, when the effect was examined at 0.4 settlement ratio, this percentage has increased to 38 % for 5° dilation soil while this percentage had been increased to 81 % for dilation angle of 10° had been chosen for the analyses.

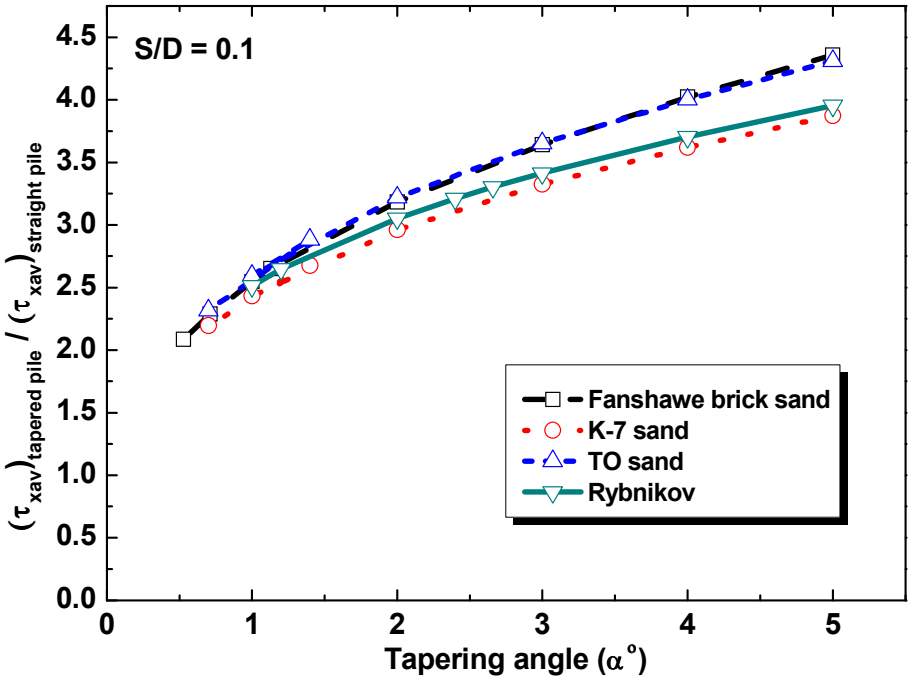

Fig. 18 Effect of angle of tapering on normalized average vertical shear stress.

After parametric studies, it is necessary to validate the proposed model with the various source of research paper accordingly. Thus, the measured and calculated results of skin friction were plotted to verify the model. The verification of the model has been accounted with various researchers' reference data accurately. The measured and predicted results of skin friction, measured in kPa with additional data from the source papers of BCP [28] and JGS [29] have been utilized. Furthermore, **Table 1** shows the database of prediction of skin friction of small model and proto type pile testing. **Figure 22** shows that the predicted model remarkably fit for evaluating unit skin frictions of tapered piles. Different types of pile geometry with different types of sandy soils have been plotted in 1:1 ratio and shows that the accuracy of proposed model validates with the parameters used.

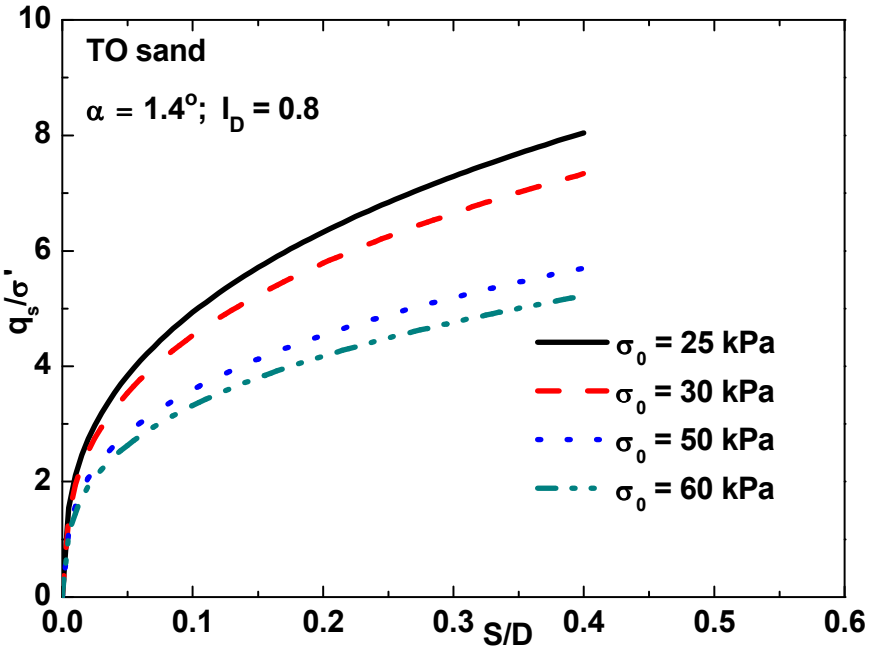

Fig. 19 Effect of initial radial stress on normalized unit skin friction.

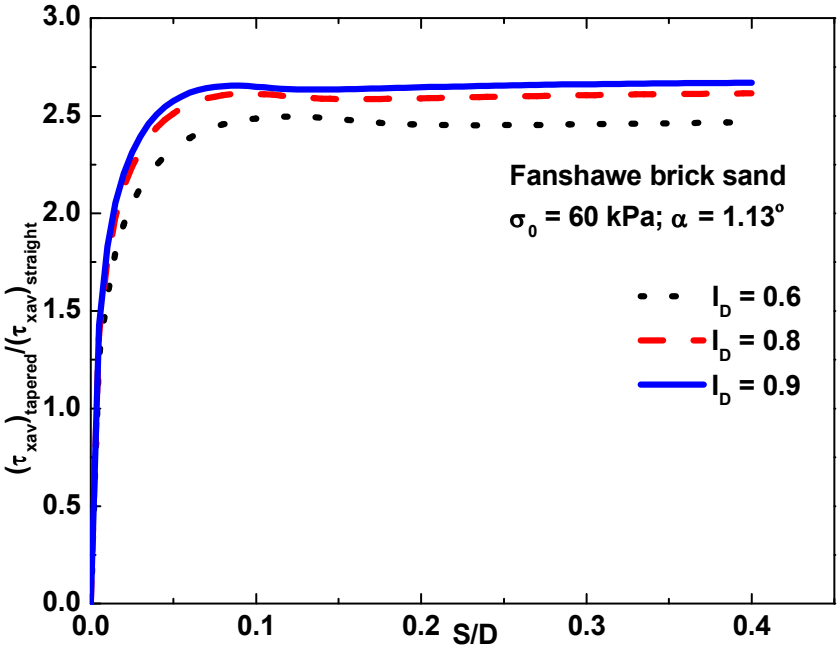

Fig. 20 Effects of relative density on average vertical shear stress.

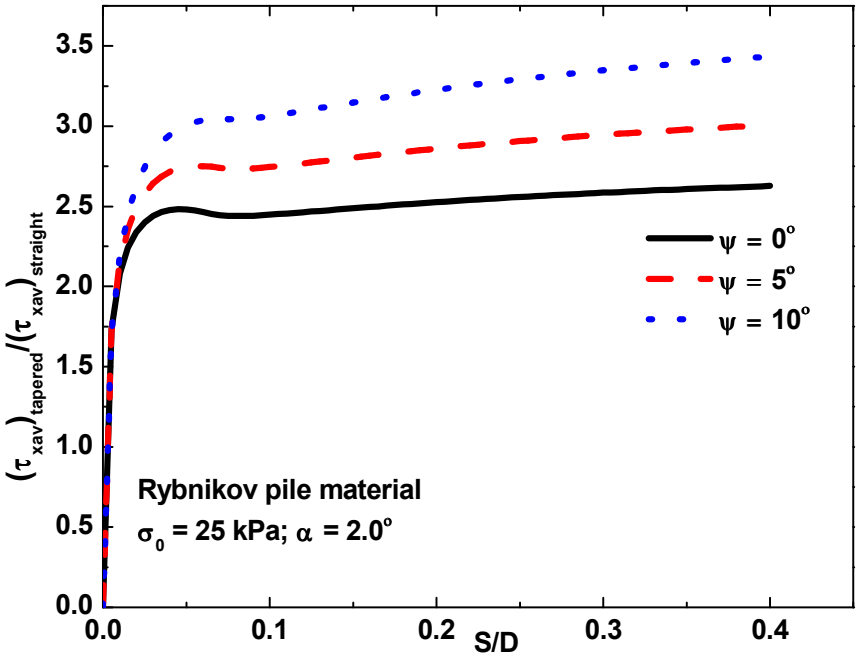

Fig. 21 Effects of dilatancy angle on normalized average vertical shear stress.

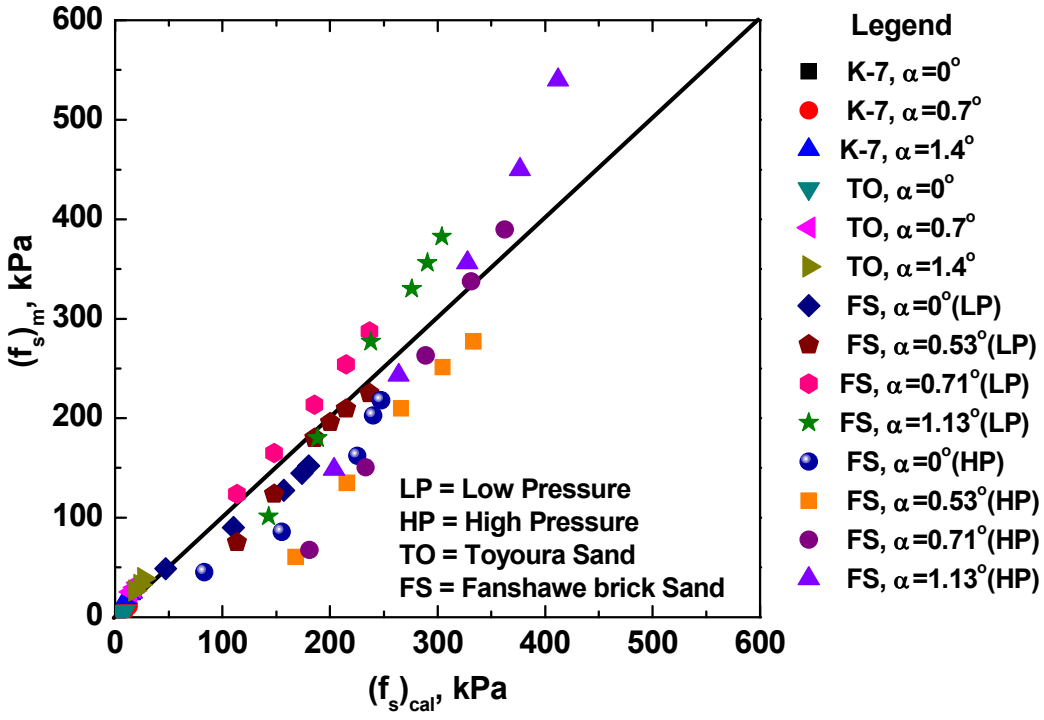

Fig. 22 Calculated and measured unit skin friction of different types of piles on different types of soil parameters.

Table 1 Prediction of skin friction in addition to different source papers.

Source Paper	Soil Type	Pile Geometry (α) ^{o}	S/D	Prediction of skin friction		
				$(f_s)_m$ (kPa)	$(f_s)_{cal}$ (kPa)	$(f_s)_m/(f_s)_{cal}$
Manandhar (2010) [13]	K-7	0	0.1	4.27	4.19	1.021
			0.2	4.00	5.05	0.791
			0.3	3.87	5.82	0.664
		0.7	0.1	6.05	9.17	0.659
			0.2	9.36	11.45	0.817
			0.3	10.69	13.02	0.821
		1.4	0.1	19.54	11.12	1.758
			0.2	23.22	14.00	1.659
			0.3	25.10	15.98	1.571
	TO	0	0.1	3.05	6.38	0.47847
			0.2	3.58	8.00	0.447
			0.3	5.87	9.05	0.648
		0.7	0.1	25.17	14.75	1.706
			0.2	29.75	18.73	1.588
			0.3	34.62	21.47	1.613
		1.4	0.1	26.66	18.24	1.462
			0.2	32.52	23.23	1.400
			0.3	39.02	26.62	1.466
Sakr et al. (2004, 2005, 2007) [22-24]	Fanshawe brick sand (LP)	0	0.025	48.60	47.03	1.033
			0.05	90.00	110.29	0.816
			0.1	127.35	157.07	0.811
			0.15	144.45	173.73	0.831
			0.2	152.10	180.04	0.845
		0.53	0.025	75.15	113.57	0.662
			0.05	123.75	147.85	0.837
			0.1	180.00	185.58	1.000
			0.15	209.25	214.94	0.974
			0.2	225.00	236.68	0.951
		0.71	0.025	101.25	142.88	0.709
			0.05	180.00	188.38	0.956
			0.1	276.75	238.01	1.163
			0.15	329.85	276.08	1.195
			0.2	382.50	303.92	1.259
		1.13	0.025	45.00	83.02	0.542
			0.05	85.50	155.31	0.551
			0.1	162.00	225.28	0.719
			0.15	202.50	240.57	0.842
			0.2	217.80	247.59	0.880
	Fanshawe brick sand (HP)	0	0.025	45.00	83.02	0.542
			0.05	85.50	155.31	0.551
			0.1	162.00	225.28	0.719
			0.15	202.50	240.57	0.842
			0.2	217.80	247.59	0.880
		0.53	0.025	60.30	168.04	0.359
			0.05	135.00	215.68	0.626
			0.1	209.70	266.22	0.788
			0.15	251.10	305.01	0.823
			0.2	277.2	333.55	0.831
		0.71	0.025	67.50	181.44	0.372
			0.05	150.30	233.44	0.644
			0.1	262.80	288.95	0.910
			0.15	337.50	331.45	1.018
			0.2	389.70	362.62	1.075
		1.13	0.025	148.50	203.74	0.729
			0.05	243.00	263.76	0.921
			0.1	356.40	327.86	1.087
			0.15	450.00	376.64	1.195
			0.2	540.00	412.20	1.310

6. Conclusions

The analytical cylindrical cavity expansion theory has been proposed to estimate skin friction of tapered piles. Stress-dilatancy relationship has been introduced to evaluate the skin friction at depth in the proposed model after carefully observed the benefits of tapered piles through evidences of small model tests and mobilized mechanism of the piles in the laboratory. The proposed models have been applied to model tests, proto type tests and real type pile tests respectively and calculated simultaneously. The main conclusions drawn from the research models are summarized as follows:

1) The mobilized mechanism has indicated that the effective radius of influenced zone around shaft of the pile increases with increasing tapering angle. As a result, convex heave on pile-ground surface have been narrowed and decreased indicating the increment of radial (or horizontal) stresses. The effective lateral pressure increment has been clearly shown by the experimental model test results also.
2) Skin frictions of tapered piles for different ground and pile geometry have shown that the slight increment on the tapering angle affects on ground with settlement ratios significantly.
3) The unit skin friction of measured and calculated results of proto type test along with various sources have been predicted and validated the proposed model.

7. Nomenclature

a	Cavity radius in cavity expansion theory
a_0	Cavity radius at zero cavity pressure
A	Constants of integration
b	Outer radius of the plastic zone during loading
c	Internal cohesion of the ground
c_i	Cohesion at pile-ground interface
D	Top diameter of tapered pile
d	Pile tip diameter
E_p	Young's modulus of pile material
F_b	Axial force at the base of pile
F_x	Axial force
f_s	Unit skin friction
G	Shear modulus
I_D	Relative density of soil
I_R	Function of relative density
I_R^o	Relative dilatancy index
K_p	Tangent gradient of pressure to radius relation
K_0	Coefficient of horizontal effective stress at rest
L	Length of the pile
n	Integer from zero to infinity
P_S	Total skin friction
p	Cavity pressure
p_0	Initial cavity pressure and in-situ hydrostatic stress
p'	Mean effective stress
r	Radius of a material point during loading
r_b	Radius of pile material at the base
r_m	Mean radius of the pile
R	Cavity pressure ratio
r_x	Radius of pile at distance x
S/D	Normalized settlement ratio
u	Radial displacement during loading measured from initial state
u_g	Vertical deformation of ground

u_p	Axial deformation of pile at distance x
$(u_p)_b$	Axial deformation of pile at base
$(u_p)_Y$	Axial deformation of pile at ground yield
v	Radial expansion of ground
x	Distance along pile from top
Y	Function of cohesion and friction angle
α	Taper angle of pile
α'	Function of friction angle
β	Function of dilation angle
γ	Function of material properties
δ	Function of material properties
η	Function of material properties
η_b	Coefficient for the depth of pile base
Λ	Infinite power series
ξ	Function of material properties
ς	Auxiliary variables
$\Delta\sigma$	Increase in radial stress at interface
ν	Poisson's ratio of ground
σ	Radial stress of ground at interface
σ_0	Initial radial stress
σ_r	Radial stress
σ_θ	Hoop stress
σ'_h	Effective horizontal stress
σ'_v	Overburden pressure
σ_Y	Stress at which ground yield due to expansion
τ_x	Average vertical shear stress
τ_0	Initial yield stress of interface
ϕ	Internal friction angle of ground
ϕ_i	Friction angle at interface
ϕ'_δ	Friction parameter
ϕ'_{cv}	Internal friction angle at critical state
ϕ'_{max}	Maximum internal friction angle

8. Acknowledgement

The authors are pleased to Professor Hemant Hazarika, Associate Professor Kiyoshi Omine, and former Assistant Professor Taizo Kobayashi for their astonishing advice. In addition, it is indebted to Laboratory Assistant Er Michio Nakashima and colleague Mr Tohio Ishimoto who has made available continuous shore up in a number of ways.

9. References

1) S. Manandhar, N. Yasufuku, et al., Response of tapered piles in cohesionless soil based on model tests, Journal of Nepal Geological Society, Vol. 40, pp. 85-92, (2010).
2) V.K. Dmokhovskii, On the Effect of the Geometric Shape of a Pile on its Capacity to resist, Tr. Moskov. Inst. Inzh. Zheleznodor. Transp., 6, (1927).
3) S. Manandhar, N. Yasufuku, et al., Skin Friction of Taper-shaped Piles in Sands, Proceedings of the ASME, 28th International Conference on Ocean, Offshore and Arctic Engineering (OMAE), Honolulu, Hawai, USA, OMAE2009-79078, pp. 93-102.

4) J.S. Horvath, and T. Trochalides, A Half Century of Tapered Pile Usage at the John F. Kennedy International Airport, to be presented at the Fifth Case History Conference on Geotechnical Engineering, New York, N.Y., U.S.A , Paper No. 11-02, (2004).
5) R.L. Norlund, Bearing Capacity of Piles in Cohesionless Soils, Journal of the Soil mechanics and Foundation Division, ASCE, Vol. 117, No. 8, pp. 1208-1226, (1963).
6) A.S Vesic`, Expansions of Cavities in Infinite Soil Mass, J. Soil Mech. Fdn. Engng Am. Soc. Civ. Engrs, Vol. 98, No. SM3, pp. 265-290, (1972).
7) M.M. Baligh, Cavity Expansion in Sands with Curved Envelopes, J. Geotech. Engng Div. Am. Soc. Civ. Engrs, Vol. 102, GT11, pp. 1131-1145, (1976).
8) J.M.O. Hughes, C.P. Wroth, et al., Pressuremeter Tests in Sands, Geotechnique, London, U.K., Vol. 27, No. 4, pp. 455-477, (1977).
9) H.S. Yu, and G. Houlsby, Finite Cavity Expansion in Dilatants Soils, Part 1, Loading Analysis, Géotechnique, Vol. 41, No. 2, pp. 173-183, (1991).
10) K.K. Kodikara, and I.D. Moore, Axial Response of Tapered Piles in Cohesive Frictional Ground, Journal of Geotechnical Engineering, ASCE, Vol. 119, pp. 675-693, (1993).
11) M.D. Bolton, The Strength and Dilatancy of Sands, Géotechnique, Vol. 36, No. 1, pp.65-78, (1986).
12) M.D. Bolton, Discussion on the Strength and Dilatancy of Sands, Géotechnique, 37, No. 2, pp.219-226, (1987).
13) S. Manandhar, Bearing capacity of tapered piles in sands, PhD Thesis, Kyushu University (2010).
14) A. Kézdi, Pile Foundation, Foundation Engineering Handbook. 1st Ed., Ed. H. F. Winterkorn and H. Y. Fang. Van Nostrand Reinhold, New York, N.Y., pp.550-600, (1975).
15) Japanese Industrial System A 1224, Japanese Geotechnical Engineering Society, 0161, The methods and description of soil tests, First revised version, pp. 59-64.
16) S. Miura, and S. Toki, A Sample Preparation Method and its Effect on Static and Cyclic Deformation-strength Properties of sand, Soils and Foundations, Japanese Geotechnical Society, Vol. 22, No.1, pp.62-77, (1982).
17) E.H. Davis, Theories of Plasticity and the Failure of Soil Masses, in Soil Mechanics, Selected Topics, ed. I.K. Lee, Butterworth, (1968).
18) M.F. Randolph, and C.P. Wroth, Analyses of Deformation of Vertically Loaded Piles, J. Geotech. Engrg., ASCE, Vol. 104, No. 12, pp.1465-1488, (1978).
19) J.D. Murff, Response of Axially Loaded Piles, J. Geotech. Engrg., ASCE, Vol. 101, No. 3, pp.356-360, (1989).
20) H. M. Coyle, and L. C. Reese, Load Transfer for Axially Loaded Piles in Clay, Int. J. Soil Mech. and Found. Div., ASCE, Vol. 92, No. 1, pp.1-26, (1966).
21) H. B. Seed, and L. C. Reese, The Action of Soft Clay on Friction Piles, Trans.ASCE, Vol. 122, pp.731-754, (1957).
22) M.Sakr, M.H. El Naggar, et al., Load Transfer of Fibre-reinforced Polymer (FRP) Composite Tapered Piles in Dense Sand, Canadian Geotechnical Journal, Vol. 41, No. 1, pp.313-325, (2004).
23) M.Sakr, M.H. El Naggar, et al., Uplift Performance of FRP Tapered Piles in Dense Sand. IJPMG-Int. Jour. of Physical Modelling in Geotechnics, Vol. 2, pp.1-16, (2005).
24) M.Sakr, M.H. El Naggar, et al., Wave Equation Analyses of Tapered FRP-concrete Piles in Dense Sand, Soil Dynamics and Earthquake Engineering, Vol. 27, pp.166-182, (2007).
25) M.H. El Naggar, M. Sakr, et al., Evaluation of Axial Performance of Tapered Piles from Centrifuge Tests, Canadian Geotechnical Journal, Vol. 37, pp.1295-1308, (2000).
26) M.H. El Naggar, M. Sakr, et al., Load Transfer of Fibre-reinforced polymer (FRP) Composite Tapered Piles in Dense sand, Canadian Geotechnical Journal, Vol. 41, No. 1, pp.313-325, (2004).
27) A.M. Rybnikov, Experimental Investigation of Bearing Capacity of Bored-cast-in-place Tapered Piles, Soil Mech. And Found. Engrg., Vol. 27, No. 2, pp.48-52, (1990).
28) BCP Committee, Field Tests on Piles in Sand, Soils and Foundations, Vol. 11, No. 2, pp.29-50, (1971).

29) Japan Geotechnical Society, JGS Standard for Vertical Load Tests of Piles, JGS, pp.151-206, (In Japanese), (1993).

Appendix I: Derivational procedure of proposed model: Stress at elastic plastic condition

Plastic zone $a \le r \le b$, after an initial yielding takes place with increment of cavity pressure p is as follows:

$$\sigma_r = \frac{Y}{\alpha'-1} + Ar^{-\frac{(\alpha'-1)}{\alpha'}} \tag{A-1}$$

$$\sigma_\theta = \frac{Y}{\alpha'-1} + \frac{A}{\alpha'}r^{-\frac{(\alpha'-1)}{\alpha'}} \tag{A-2}$$

Where, A is a constant of integration.

$$A = -\frac{2\alpha'(Y+(\alpha'-1)p_0)}{(\alpha'-1)(1+\alpha')}b^{\frac{(\alpha'-1)}{\alpha'}} \tag{A-3}$$

Also at two boundary conditions:

$$\sigma_r(a) = -p \tag{A-4}$$

$$lim_{r\to\infty}\,\sigma_r = -p_0 \tag{A-5}$$

Combining Eq. (A-4) and (A-1) to express the cavity pressure ratio R and current cavity radius a as below:

$$-p = \frac{Y}{\alpha'-1} + \left\{-\frac{2\alpha'(Y+(\alpha'-1)p_0)}{(\alpha'-1)(1+\alpha')}b^{\frac{(\alpha'-1)}{\alpha'}}\right\}a^{-\frac{(\alpha'-1)}{\alpha'}}$$

$$p + \frac{Y}{\alpha'-1} = \frac{2\alpha'(Y+(\alpha'-1)p_0)}{(\alpha'-1)(1+\alpha')}\left(\frac{b}{a}\right)^{\frac{(\alpha'-1)}{\alpha'}}$$

$$p + \frac{Y}{\alpha'-1} = \frac{2\alpha'(Y+(\alpha'-1)p_0)}{(\alpha'-1)(1+\alpha')}\left(\frac{b}{a}\right)^{\frac{(\alpha'-1)}{\alpha'}}$$

$$\left(\frac{b}{a}\right)^{\frac{(\alpha'-1)}{\alpha'}} = \frac{(1+\alpha')(Y+(\alpha'-1)p)}{2\alpha'(Y+(\alpha'-1)p_0)}$$

$$R = \frac{(1+\alpha')(Y+(\alpha'-1)p)}{2\alpha'(Y+(\alpha'-1)p_0)} \tag{A-6}$$

The mean effective stress is given by:

$$p' = \frac{\sigma_r+\sigma_\theta}{2} \tag{A-7}$$

Substituting values of σ_r and σ_θ from Eqs. (A-1) and (A-2) into (A-7) and deriving step by step as follows:

$$p' = \frac{1}{2}\left[\frac{Y}{\alpha'-1} + Ar^{-\frac{(\alpha'-1)}{\alpha'}} + \frac{Y}{\alpha'-1} + \frac{A}{\alpha'}r^{-\frac{(\alpha'-1)}{\alpha'}}\right] \tag{A-8}$$

$$= \frac{1}{2}\left[\frac{2Y}{\alpha'-1} + \frac{A}{\alpha'}r^{-\frac{(\alpha'-1)}{\alpha'}}(1+\alpha')\right]$$

$$= \frac{Y}{\alpha'-1} + \frac{A}{2\alpha'}r^{-\frac{(\alpha'-1)}{\alpha'}}(1+\alpha')$$

From Eq. (A-3) and validating Eq. (A-4) to get the following results:

$$p' = \frac{Y}{\alpha' - 1} + \left\{ \frac{-2\alpha'(Y + (\alpha' - 1)p_0)}{(\alpha' - 1)(1 + \alpha')} \left(\frac{b}{a}\right)^{\frac{(\alpha'-1)}{\alpha'}} \frac{(1 + \alpha')}{2\alpha'} \right\}$$

$$p' = -\left(\frac{b}{a}\right)^{\frac{(\alpha'-1)}{\alpha'}} \frac{(\alpha' - 1)}{(\alpha' - 1)}$$

$$p' = -p_0 R \tag{A-9}$$

Appendix II: Computational procedure of skin friction of tapered piles using load transfer method

1. Assume pile into *n*-segments from base to top as *1, 2, ..., (n-1), n*. Value of radial expansion at midpoint of each segment $v_1 = v_2 = v_n = 0$.
2. Assume small displacement at pile base $(u_p)_b$.
3. Compute base load F_b correspond to $(u_p)_b$ using $F_b = \frac{4r_0 G}{(1-\nu)\eta_b}(u_p)_b$. For side-only piles, $F_b = 0$.
4. Set load at the base of 1st segment $(u_p)_1^b$ to $(u_p)_b$.
5. Set segment counter *i* to *1*.
6. Make 1st estimate of the midpoint deformation $(u_p)_i$ of segment *i*: $(u_p)_i = (u_p)_i^b$.
7. Estimation of average vertical shear stress τ_x at the midpoint of the segment:

A. If $(u_p)_Y \geq (u_p)_i > (\zeta r_m/G)\tau_0$ then If $(u_p)_i \leq (\zeta r_m/G)\tau_0$, estimate $\tau_x = \frac{G}{\zeta r_m} u_p$ and set $v = 0$.

Estimate, $\tau_x = \frac{K_e \tan\alpha \tan(\alpha+\varphi_i) u_p + \sigma_0 \tan(\alpha+\varphi_i) + c_i'}{1 + \frac{K_e \zeta r_m}{G} \tan\alpha \tan(\alpha+\varphi_i)}$

Update v and σ using $v = (u_p - u_g)\tan\alpha$ *and* $\Delta\sigma = \frac{2G}{r_m}$.

B. If $(u_p)_i > (u_p)_Y$

a. Estimate v as: $v = u_p \tan\alpha - \frac{\zeta r_m}{G}\tan\alpha\, \tau_x$.

b. Compute dv for this increment using $dv = v - v_i$.

c. Compute $K_p = \frac{1}{A}\frac{1}{C}\frac{\beta+1}{\beta}\left(\frac{a}{a_0}\right)^{(\beta+1)/\beta}\frac{1}{a}$, and $\left[\frac{a}{a_0}\right]^{(\beta+1)/\beta} = \frac{R^{-\gamma}}{(1-\delta)^{(\beta+1)/\beta - \frac{\gamma}{\eta}} A(R,\xi)}$.

d. Compute $d\sigma = K_p - dv$.

e. Update σ.

f. Compute $\tau_x = \left(\sigma_Y + \int_{vY}^{v} K_p\, dv\right)\tan(\alpha + \varphi_i) + c_i'$.

8. Compute load on top of the segment *i*, $F_i^t = F_i^b + \tau_x \Delta L (2\pi r_i^m)$.
9. Compute the elastic deformation in the bottom half of the segment *i*, $\Delta(u_p)_i^t = \frac{\frac{F_i^m + F_i^b}{2}\frac{\Delta L}{2}}{A_i^b E_p}$ and, $F_i^m = \frac{F_i^t + F_i^b}{2}$.
10. Compute the new midpoint deformation of the segment *i*, $(u_p)_i^{new} = (u_p)_i^b + \Delta(u_p)_i^b$.
11. Compare the new estimate of midpoint deformation $(u_p)_i^{new}$ with $(u_p)_i$. If not agree, set $(u_p)_i = (u_p)_i^{new}$, return to step (7).
12. Compute $\Delta(u_p)_i^t = \frac{\frac{F_i^m + F_i^t}{2}\frac{\Delta L}{2}}{A_i^t E_p}$, and $(u_p)_i^t = (u_p)_i + \Delta(u_p)_i^t$.
13. If $i < n$, set F_{i+1}^b to F_i^t, u_{i+1}^b to u_i^t, v_i to v and *i to i+1* and return to step (6). Otherwise F_n^t is the load at the pile top, and u_n^t is the deformation.
14. Increment the base displacement $(u_p)_b$ and return to step (3) for complete load-deformation.